ELSEVIER

Nuclear Engineering and Design 188 (1999) 49–73

Nuclear Engineering and Design

An experimental investigation on thermal striping Mixing phenomena of a vertical non-buoyant jet with two adjacent buoyant jets as measured by ultrasound Doppler velocimetry

A. Tokuhiro *, N. Kimura

Reactor Engineering Section (RES), Safety Engineering Division (SED), Oarai Engineering Center (OEC), Power Reactor and Nuclear Fuel Development Corp. (PNC), 4002 Narita, Oarai-machi, Ibaraki, 311-1393, Japan

Received 13 March 1998; received in revised form 5 May 1998; accepted 29 December 1998

Abstract

An experimental investigation on the thermal mixing phenomena of three quasi-planar vertical jets, with the central jet at a lower relative temperature than the two adjacent jets, was conducted. The central jet was unheated ('cold'), while the two adjacent jets were heated ('hot'). The temperature difference and velocity ratio between the heated (h) and unheated (c) jets were, $\Delta T_{hc} = 5°C$, $10°C$ and $r = V_{cold,exit}/V_{hot,exit} = 1.0$ (isovelocity), 0.7, 0.5 (non-isovelocity) respectively. The typical Reynolds number was $Re_D = 1.8 \times 10^4$, where D is the hydraulic diameter of the exit nozzle. Velocity measurement of a reference single-jet and triple-jet arrangement were taken by ultrasound Doppler velocimetry (UDV) while temperature data were taken by a vertically traversed thermocouple array. Our UDV data revealed that, beyond the exit region, our single-jet data behaved in the classic manner. In contrast, the triple-jet exhibited, for example, up to 20 times the root-mean-square velocity values of the single-jet, especially in the regions in-between the cold and hot jets. In particular, for the isovelocity case ($V_{exit} = 0.5$ m/s) with $\Delta T_{hc} = 5°C$, we found that the convective mixing predominantly takes place at axial distances, $z/D = 2.0–4.5$, over a spanwise width, $x/D \sim |2.25|$, centered about the cold jet. An estimate of the turbulent heat flux distribution semi-quantitatively substantiated our results. As for the non-isovelocity case, temperature data showed a localized asymmetry that subsequently delayed the onset of mixing. Convective mixing however, did occur and yielded higher post-mixing temperatures in comparison to the isovelocity case. © 1999 Elsevier Science S.A. All rights reserved.

* Corresponding author. Tel.: +81-29-267-4141; fax: +81-29-266-3718.
E-mail address: kimura@oec.jnc.go.jp (N. Kimura)

PII: S0029-5493(99)00006-0

1. Introduction

Thermal striping refers to random thermal cycling of reactor structures and components as a result of fluid–structure interaction; that is, striping is likely a description of the cold and hot (thermal) stripes appearing as plumes and jets, that a solid boundary must withstand due to preferential or inefficient mixing of coolant flowing through and exiting the reactor core. The net result of striping is undesirable since thermal fatigue of materials can lead to structural and material failure. Thermal striping as a phenomenological problem in LMFBRs was already recognized in the early 1980s by Wood (1980) and Brunings (1982) and has subsequently been considered by Betts et al. (1983), Moriya et al. (1991), Muramatsu (1994) and Tokuhiro (1996).

We note here that, although the phenomena taken as a whole involve fluid–structure interaction, the analytical and experimental efforts have traditionally been divided into separate structural and thermal-hydraulic investigations. In the present work, we focus strictly on the thermal-hydraulic aspects; that is, mainly the convective mixing of a multiple number of jets at different temperatures and average exit velocities. In the past, investigations on jets have encompassed the single-jet, which has most extensively been studied, to two jets flowing side-by-side, at a relative angle or co-axially and with a relative velocity (and/or temperature) with respect to each other. In fact, in the LMFBR sector, co-axial jets of sodium have been investigated by Tenchine and Nam (1987) while Tenchine and Moro (1995) compared the results of sodium and air jet experiments. Investigations of more than two jets seem to be rare. Thus besides its relevance to LMFBR thermal-hydraulics, a study of a multiple number of vertical jets at either the same or different densities (temperatures), may be of general interest to the heat transfer community.

In the present study, we carried out water-based experiments in a test facility simulating the mixing of one centrally located, unheated jet sandwiched by two adjacent jets either buoyant (at higher temperature) and/or at different exit velocity relative to the central jet. The three-jet arrangement is a simplified simulation of hot and cold flow channels in a LMFBR core. An understanding of thermal striping or rather the convective mixing is one of the key issues in the safe design of the LMFBR. Experimentally, one objective of the study was to demonstrate the applicability of the ultrasound velocity profile (UVP) monitor for velocity measurements. By applicability we mean velocity measurements in the flow field of relevance. Subsequently, we first obtained and evaluated the hydrodynamic information concerning the nature of mixing between thermally-stratified jets. Then with the addition of temperature data we were able to assess the thermal-hydraulics of mixing process.

2. Experiment

2.1. Experimental facility

Fig. 1 shows the experimental loop including the test section. Except for the test section, the

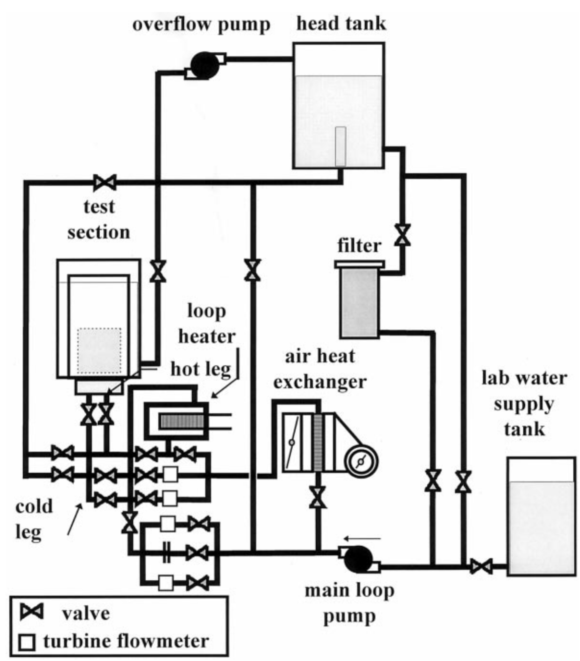

Fig. 1. Schematic of experimental loop.

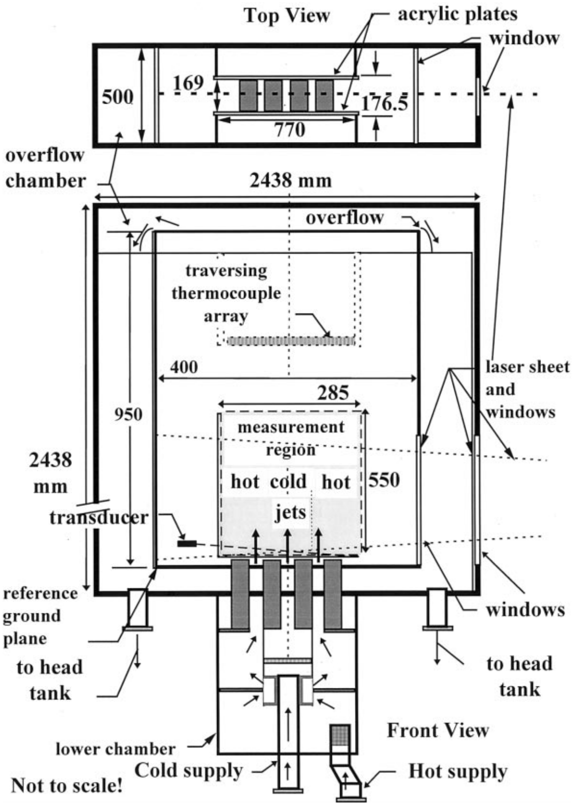

Fig. 2. Schematic of test section.

rest of the facility functions as a support system shared by two other experiments. The facility thus consists of the thermal striping test section set within a larger rectangular tank, a loop heater/exchanger for supplying hot water, a head tank in order to control the water level, a filter to extract contaminants within the loop, an air-to-loop heat exchanger for supplying cold or cooled water back into the loop and finally a general purpose laboratory water supply tank. Several turbine flowmeters as well as orifice plate type devices, a system of valves and all the connecting piping are as depicted.

A more detailed view of the test section itself is shown in Fig. 2. The test section is immersed within a rectangular tank measuring 2438W × 2438H × 671D (W is width, H is height, D is depth, all mm), and the test section itself is a partially enclosed rectangular region measuring 400W × 950H × 176.5D. As noted in the top view, two acrylic plates sandwich the four rectangular blocks thereby restricting the spread of the exiting jets in these directions. The rectangular blocks and plates defined three exits, each measuring 50 × 176.5 mm. The equivalent hydraulic diameter was $D = 35.7672$ mm. The idea was to constrain the jet to a finite width and to 'view' it as quasi two-dimensional (planar) within this geometry. The right and left sides are open so that even with an overflow mechanism at the top of the test section there may be some recirculating flow through the sides. A prominent feature of the tank is the large viewing glass windows on both the front, back and right side of the tank. This feature was included primarily for laser-based measurements and flow visualization techniques. Below the test section are three rectangular channels defined by four equally rectangular blocks. The central channel functions as the 'cold' jet supply while the adjacent two are 'hot'. The hot and cold jets are supplied from separate sources, the cold source being centrally situated, flowing first through an expansion, a grating and then through a flow constriction. The hot source is on the other hand supplied from the right-hand-side into a lower chamber. The flow then weaves its way past the cold pipe and enters symmetrically through a one-sided rectangular constriction. The exit of the nozzle is a block elevated 45 mm from the reference groundplane of the tank.

The other prominent components of the test facility is the traversing thermocouple array and the ultrasound transducer holder affixed to the left arm of the traversing mechanism. A schematic is shown in Fig. 3 along with the exit blocks. The moving mechanism consists of two vertical and parallel pillars (OD 45 mm; only left is shown), between which a 'bridge' served as a mounting bracket for thermocouples. This bridge is fixed and moves up and down with the pillars. The pillars are traversed externally from above the tank by an electric motor. The traversing thermocouple array consists of 39 thermocouples (T/Cs) facing vertically downward and horizontally spaced 5 mm apart over a 190 mm span. The last 5 mm of each of the 39 thermocouples are directly exposed to the flow, while beyond this point the T/C is insulated for a length of 50 mm. The T/Cs are threaded and bonded to the horizontal bridge and the lead wires are contained either in the right or left pillars. The two arms exit out the top of the rectangular tank. The thermocouple are T-type, constantan copper–nickel with an expected measurement error of 0.5°C. Operationally three T/Cs malfunctioned (Nos. 5, 6, 14, numbering from left) and could not be used for data acquisition.

Velocity measurements were taken using the Met-Flow Model X-1 ultrasound velocity profile (UVP) monitor (Met-Flow SA, Lausanne, Switzerland) with a single, Delrin-encased (temperature limit ~ 80°C) piezo-electric transducer operating at 4 MHz. The transducer had an ultrasound beam diameter of 6 mm with a beam spreading angle of approximately 3° over 75 cm. The UVP is an ultrasound Doppler velocimeter, working on the principle of echography; that is, the position and velocity information are evaluated respectively from the detected time-of-flight and the Doppler-shift frequency at the detected position, within each of 128 ‘coin-like’ volumetric elements along the beam’s path, during 1024 time intervals. Thus at each time interval, a componental velocity profile, based on 128 points, is constructed along the measurement line (ML) of the ultrasonic beam. By componental it is understood to mean that the velocity vector oriented either toward or away from the face of the transducer, determined(from the sign of the Doppler shift. The real-time corresponding to 1024 measurement intervals is adjustable depending largely upon the preference (and experience) of the user, though it should be based on the phenomenon of interest in the flow; that is, based on estimates of the time-scales associated with various transport phenomena, the user is able to select either a short or long time span between measurements. The UVP can thus detect time-dependent phenomena during a minimum time-span of 30 ms to minutes and hours. The device has been developed and tested in thermohydraulic applications, most notably by Takeda (1986, 1991, 1993).

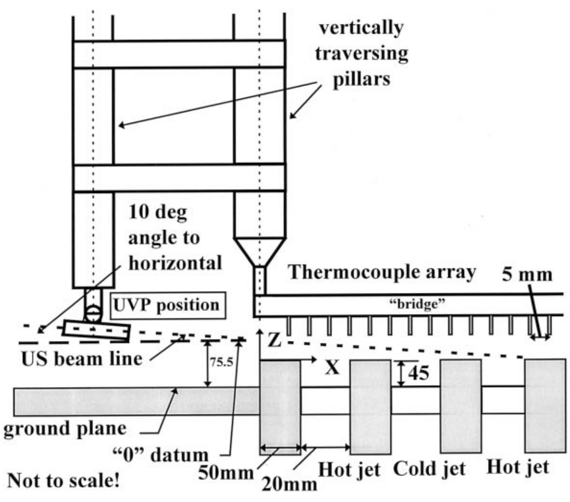

Fig. 3. Schematic of instrumentation set-up. Close-up of the UVP transducer orientation and traversing thermocouple array.

The ultrasound is reflected from tracer particles, typically a plastic powder with a nominal size of 50–100 μm ($\rho = 1.02$ kg/m^3), that are added to the test medium (water). One should note that the inherent assumptions in using this measurement technique are that: (1) the tracer particles accurately reflect the velocity profile of the liquid state and (2) the modification of the flow field due to addition of tracer particles; that is, the particle–fluid interaction, is of minor consequence to the measured profile. Additionally, it is assumed that particle-to-particle interactions are negligible. We realized this by using a low concentration of tracer particles, on the order of 100 g per 4000 l (3988) of water. Finally, regarding the former, we assume that there is no slip (relative) velocity between tracer particle and liquid; that is, the particle moves exactly as a fluid element would, as dictated by the initial and boundary conditions of the flow. As for the positioning of the transducer, it was held in place by a short piece of pipe through which the transducer was inserted (and held) while the output signal traveled through a 4 m long cable. The typical measurement time for 128 spatial $\times$ 1024 temporal points, was on the order of 1–3 min.

2.2. Conditions of UVP and temperature measurements

For the data presented in this paper, the average exit velocity of both the single- and triple-jet

Table 1
Experimental conditions

Case	T05 V0505	T05 V1010	T10 V0505	T10 V1010	T05 V1005	T10 V1005	T10 V1007	T05 V1007
Hot jets								
Velocity (m/s)	0.5	1.0	0.5	1.0	1.0	1.0	1.0	1.0
Temperature (°C)	30	35	42	42	30	40	40	32
Cold jets								
Velocity (m/s)	0.5	1.0	0.5	1.0	0.5	0.5	0.7	0.7
Temperature (°C)	25	30	32	33	25	30	30	27
Discharged temperature difference (°C)	5	5	10	9	5	10	10	5
Discharged velocity ratio W_{cold}/W_{hot}	1.0	1.0	1.0	1.0	0.5	0.5	0.7	0.7

configurations were 0.5, 0.7, 1.0 or 2.0 m/s with an estimated error of 0.1 m/s. The temperature difference between the cold and each of the hot jets was either 5°C or 10°C in all cases with an estimated, conservative error of 0.75°C. UVP measurements were conducted with the transducer fixed at either the right (R) or left (L) locations with respect to the jet(s) (see Figs. 2 and 3). Measurements were taken axially, along the z-axis, at 5-mm intervals up to approximately 550 mm above the imaginary '0'-plane in most cases. For all the data present here, the UVP transducer was oriented at an angle of 10° with respect to the horizontal. The selection of the 10° angle was an experimental compromise between having a sufficient number of axial locations, which we sought in order to follow the flow development, and the inclusion of the larger, axial vector component relative to the horizontal component of the actual jetting flow. Table 1 summarizes the experimental conditions covered in this paper. UVP measurements were restricted to case T05V0505.

3. Results and discussions

3.1. Photographs and video images

We first present in Fig. 4(a) and (b) digitized image sequences of respectively, the single- and triple-jets extracted from video as a qualitative introduction. The images have been taken with laser-sheet (argon laser) illumination from the right side with Rhodamine dye added to water. An horizontal line tracing the laser sheet beam is clearly visible on the top surface of the four blocks. Fig. 5 depicts a typical frame-by-frame sequence of the triple-jet at different average exit velocity and temperature difference conditions. Note that qualitatively some flow structures are evident and that some contrasts such as in characteristic lengths appear in (a), (b) and (c). Since a normal speed video camera was used to record these images, some fast flow phenomena could not be captured. Nevertheless, it is clear from the figure that our triple-jet has a spatial (x,z) and temporal (time) dependence. Note that in the present set-up the axial coordinate is the z-axis (streamwise) and the spanwise (transverse) distance is the x-axis. Finally in order to facilitate our presentation, we refer to the buoyant jets as the 'hot' jets and the non-buoyant, central jet as the 'cold' jet.

3.2. UVP velocity profiles: single-jet and triple-jet

Fig. 6(a) shows a representative set of average velocity profiles of the single-jet at z-locations taken by the UVP. The profile shown is that of the velocity component at 10° to the horizontal;

that is, nearly the spanwise component. The profiles have been chosen to clearly display the changes with downstream locations. The abscissa depicts the 128 channels (0–127) along the ultrasound beam, a distance equivalent to 284 mm, with the centerline taken as the origin ($x/D = 0$). In Fig. 6(b) we show one profile (at $z = 45$ mm) and its associated standard deviation profile in order to explain details of the profile itself. The actual profile as measured by the transducer depicted in Fig. 3 is the inverted image of Fig. 6(b); that is, recall that with respect to the transducer, flows coming toward it are '−' (negative) and those flowing away are '+' in terms of the sign of the Doppler shift. The inverted profile does not, however, change in any way the information content of the depicted velocity profile. We thus see that a prominent feature is the peaked, jet-like profile in the central region. Additionally, to either side of the center is the entrained-flow regions which show flow of approximately equal magnitude and on-average of opposite sign with

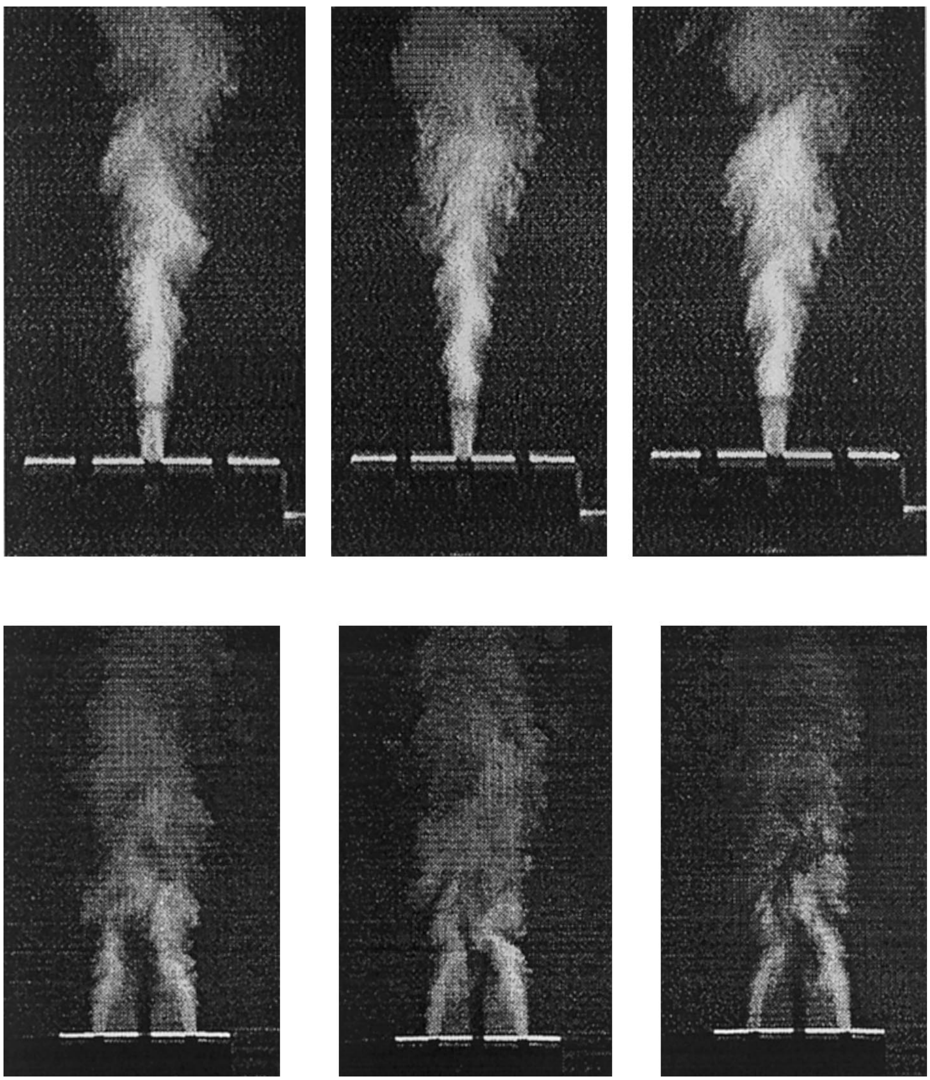

Fig. 4. (a) A sequence of three snapshot images digitized from video of the single-jet. (b) A sequence of three snapshot images digitized from video of the triple-jet.

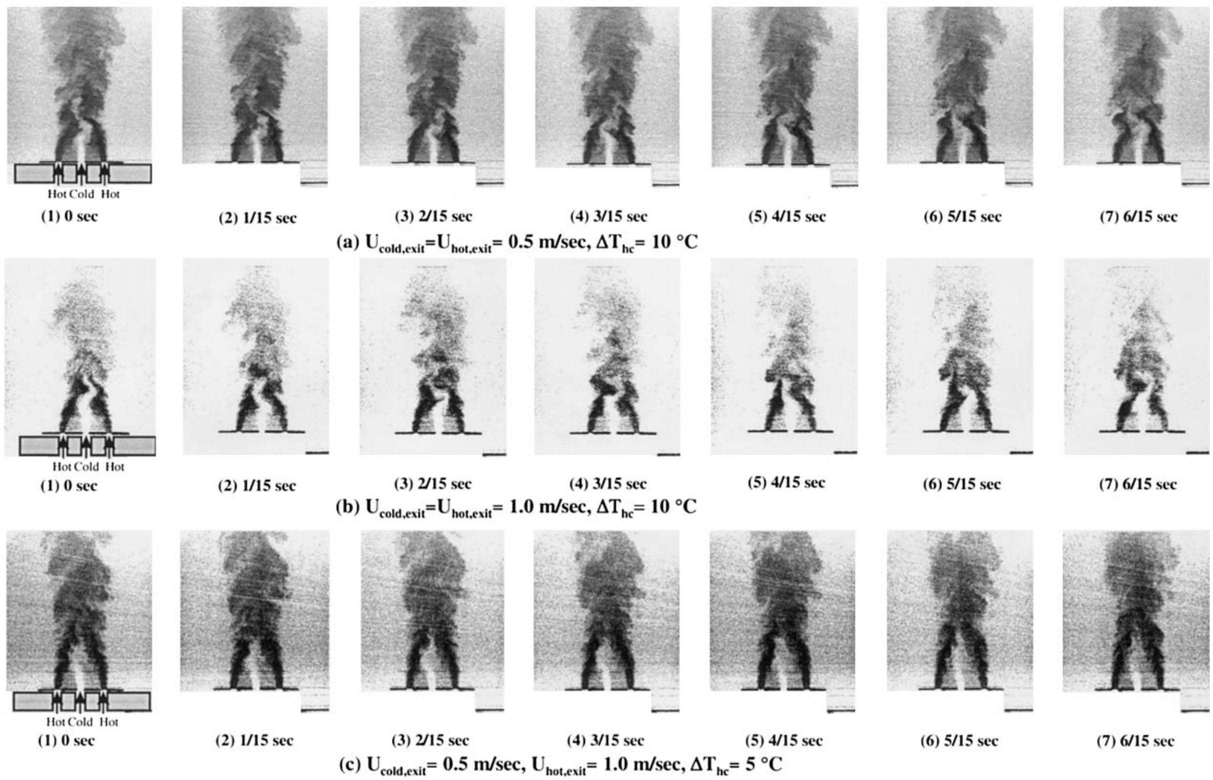

Fig. 5. Digitized images of the triple-jet under various experimental conditions at 1/15th s intervals.

respect to the transducer. We say on-average here because the entrained flow, to either side of center, not only flow in opposite directions, but fluctuates in magnitude during the measurement period. We observed this while analyzing sets of 1024 profiles. Finally in Fig. 6(b) the standard deviation distribution, perhaps describable as twin peaks and a valley, characterizes and denotes the edge and core of the jet.

As a measure of validation of our (isothermal) single-jet data with that from past investigations we compare in Fig. 7(a) the axial decay of the centerline velocity, measured by both ultrasound (UDV) and laser (LDV) Doppler velocimetry, against past data represented as lines. The UDV data taken using the UVP represents data taken at $U_o = 0.5$ m/s and with the transducer at the right (R). The LDV data were taken at $U_o = 1$, 2 m/s. The past data were extracted from Kataoka (1986) and are represented by linear regression lines above the so-called velocity core length, z_{uc}. The core length corresponds to the axial location below which the data assumes a quasi-constant value ($z_{uc} \sim 4$). To the best of our knowledge the past data are for isothermal gas (air and methane) jets. Note that there are variations in slope and magnitude even for identical gases. Except for the exit region ($z < 0.8$) for which Kataoka presents no data and one point at $z/D \sim 11$, our data are consistent with past investigations. Fig. 7(b) next shows a comparison of average velocity profiles of U_x, at approximately the same z-locations, measured by UDV (lines) and LDV (symbols). The agreement, though between $U_o = 1.0$ m/s for LDV and $U_o = 0.5$ m/s for UDV, is generally satisfactory for $x/D \leq |1|$. The difference is in the entrained flow region in which the UDV profile contains directional (+and −) values in the shown average. Because the spanwise distance, x/D, at which there is uni-directionality in flow cannot be discriminated from the contrary (except by ad-hoc means), the UDV profile here remains as measured.

Fig. 8(a) and (b) show a representative set of average velocity profiles of the triple-jet at several axial locations, coincidental to those in Fig. 6(a). As before, the velocity component measured is at 10° with respect to the horizontal; thus nearly the transverse component. Due to the number of jets (3), the individual profiles are much more difficult to discern here than in Fig. 6(a). Nevertheless the change in the profile from $z = 45$ to $z = 170$, then

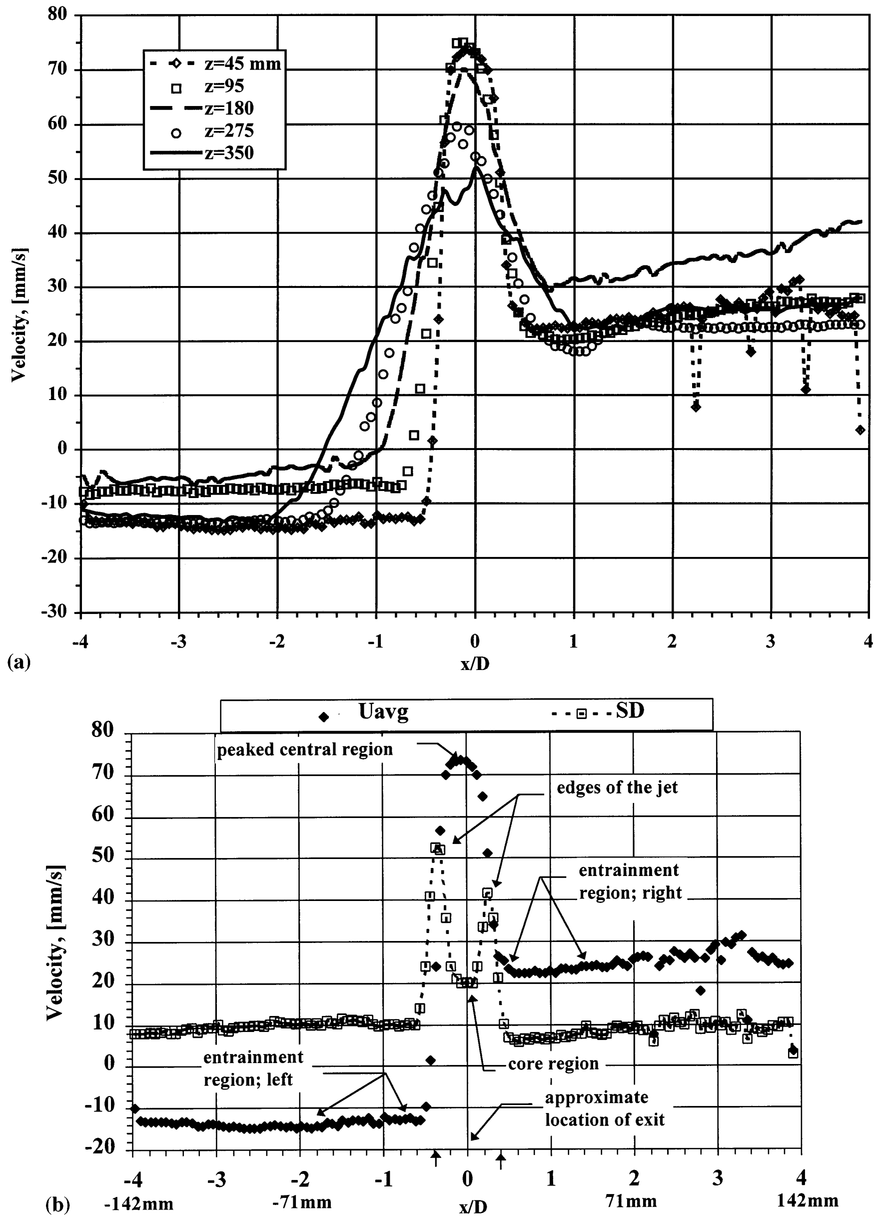

Fig. 6. (a) Average velocity profile of the single-jet at selected axial locations. (b) Average velocity and standard deviation profiles of the single-jet at $z = 45$ mm from the exit.

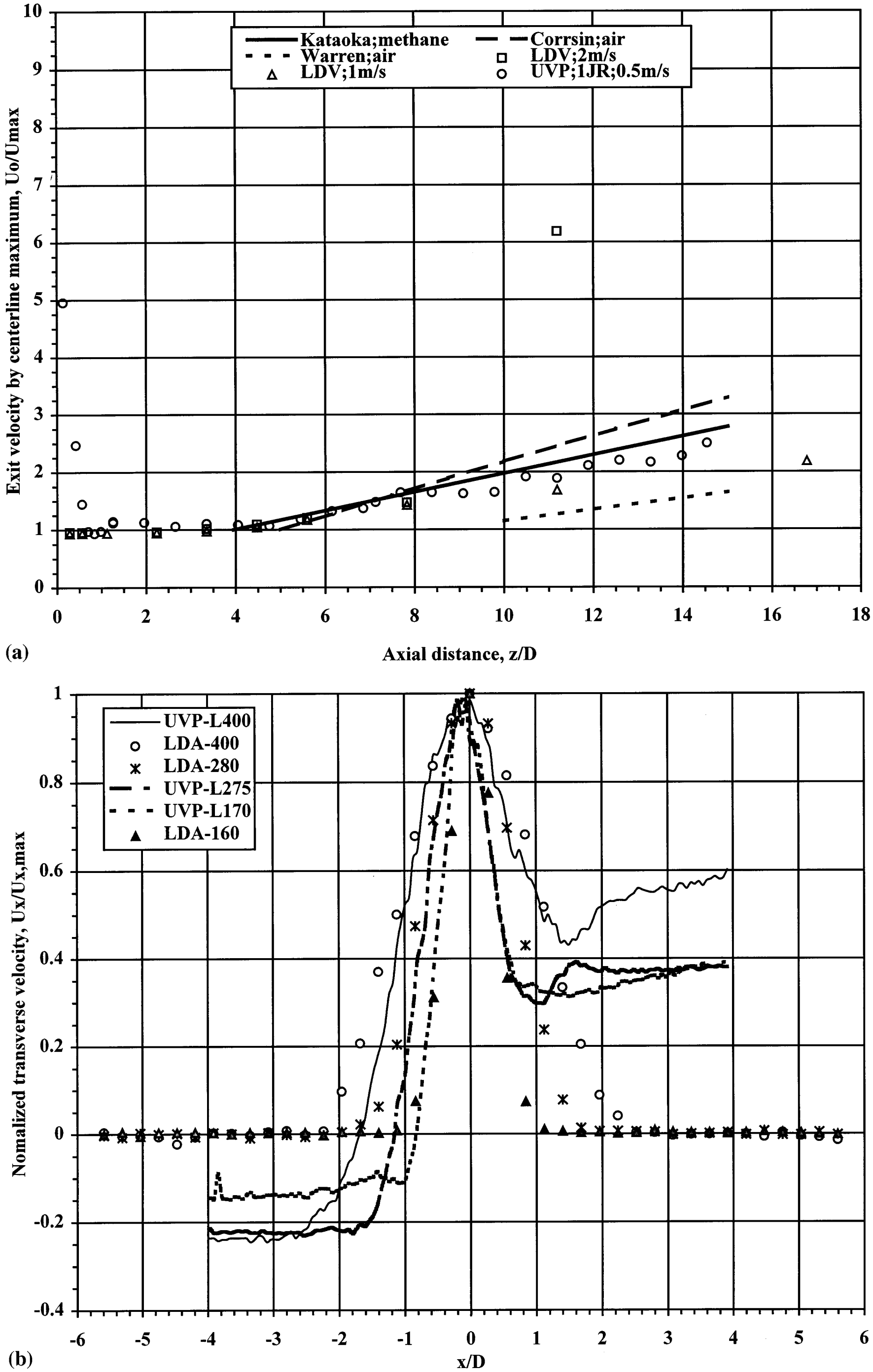

Fig. 7. (a) Comparison of past correlations, LDV and UVP measured centerline decay velocity. (b) Comparison of velocity profiles taken by LDA and UVP at selected locations.

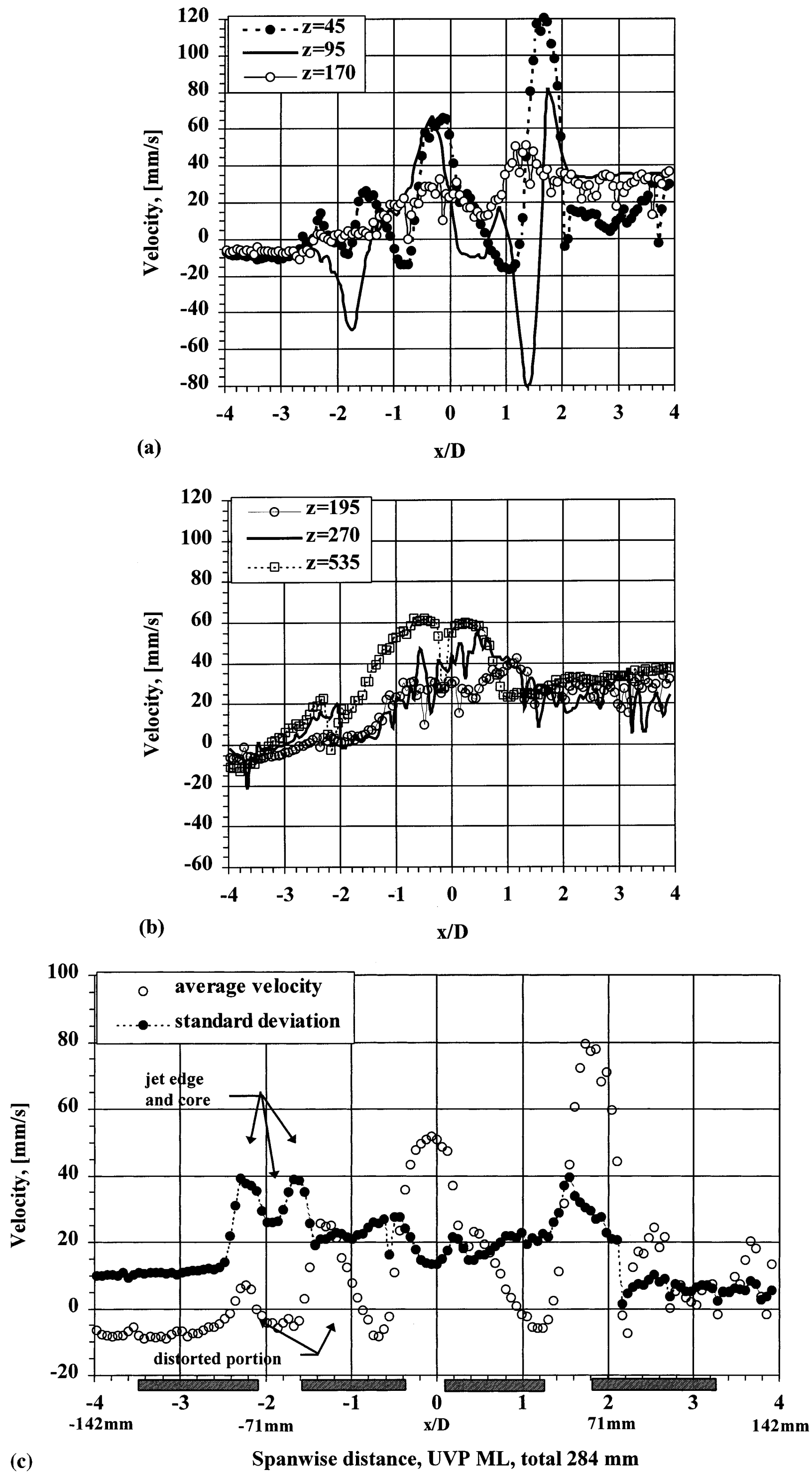

Fig. 8. (a, b) Average velocity profile of the triple-jet at selected axial locations. (c) Average velocity and standard deviation profiles of the triple-jet at $z = 45$ as taken from the right (R). (d) Qualitative sketch of idealized triple-jet velocity profile and features.

to $z = 535$ is clear; the 'peaky' profiles in (a), due to mixing, assume a 'composite jet-like' profile (beyond where the jets merge in Fig. 5) in (b). In Fig. 8(c) at $z = 45$ the standard deviation profile depicts the edges and core of each jet, clearly at the left, center and slightly distorted at right. The average velocity on the other hand revealed a distorted profile at the jet closest to the transducer, whether measured from the right or left, while the remaining two jets depict a trend similar to the idealized profile shown in Fig. 8(d). It is our judgment that this distortion is due either to inadequate amplification of the echoes returning from the tracer particles and/or the existence of acoustic beam 'side-lobes' from the transducer, that 'locally' (where distortion exists) perturb the calculation of the average. The acoustic beam is ideally an oblong (elliptical) beam along the measurement line (ML), spanning in this case some 75 cm. The so-called side-lobes are equally elliptical, but at some acute angle with respect to ML. If the amplification of the channels corresponding to the (near) jet region is inadequate or particles within the side-lobes add significantly to the echo signal, we would not expect a profile as in Fig. 8(d). This discrepancy is under investigation and as such we have not drawn conclusions depending substantially on this data.

Fig. 9 shows the calculated root mean square (RMS) velocity distribution versus axial distance for both the single-jet (1J) and triple-jet (3J), the latter for both left (L) and right (R) UVP transducer orientations. The triple-jet data were taken on two different occasions so that although operational conditions were nearly identical, it is likely that thermohydraulic conditions were not exactly reproduced. The single-jet data are for an isothermal jet. The average exit velocity in all three cases was 0.5 m/s. While there are some differences in the triple-jet data the striking contrast is between the single- and triple-jets. In fact the triple-jet reaches values larger than what one might expect

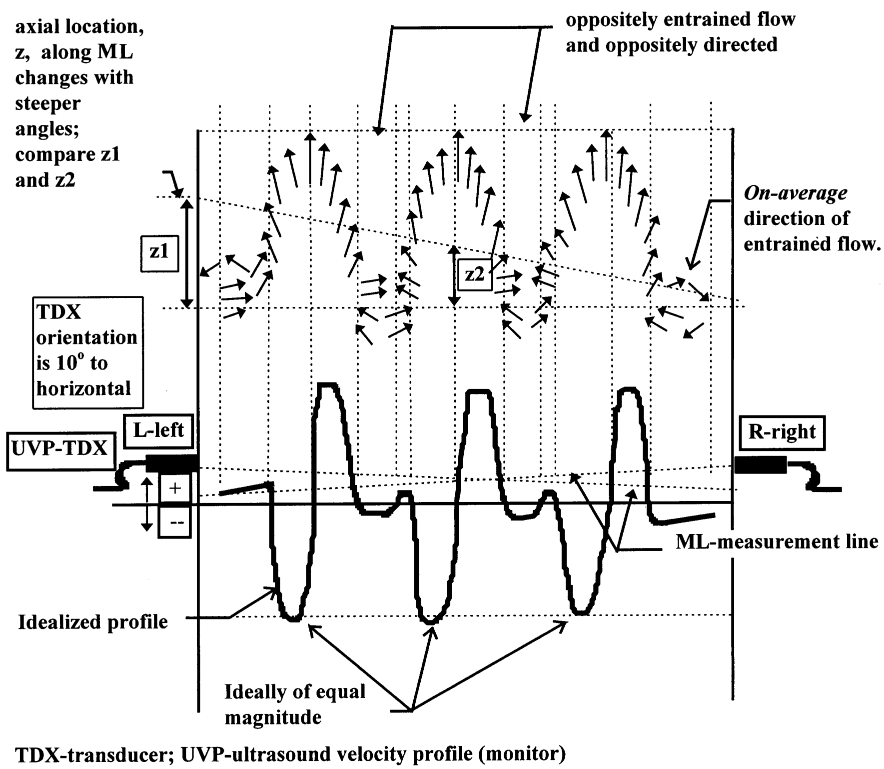

Fig. 8. (*Continued*)

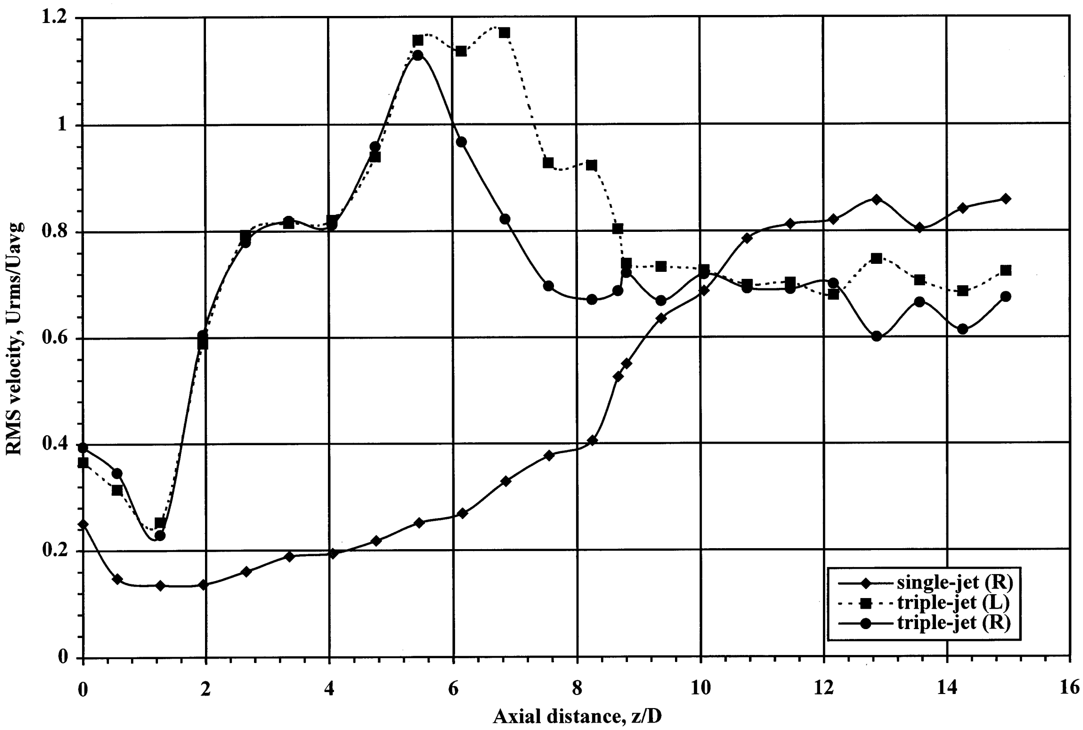

Fig. 9. Comparison of the RMS of velocity versus axial distance of single- and triple-jets.

as a 'rule-of-thumb'; that is, roughly three times the single-jet value (see $2 < z/D < 7$). Furthermore, the overall trend is different than the single-jet, which in comparison steadily increases up to $z/D \sim 11$ where it appears to reach a quasi-constant value. We note that in Gebhardt et al. (1988) the fully turbulent region of an isothermal (or non-buoyant) axisymmetric (single) jet, as characterized by the axial distribution of the turbulent intensity, is reached at approximately 10 diameters downstream from the exit. If we were to expect our quasi-planar jet to behave similarly, then for $Re \sim 2 \times 10^4$ where $Re = U_{\mathrm{av,exit}}D/\nu$, our datum points have yet to reach a fully turbulent state. Equally, that our largest values are reached at $z/D \sim 15$ is different from the quoted work. The triple-jet in contrast, beyond a local minimum at $z/D \sim 1.2$, shows a rapid increase to a maximum value at $z/D \sim 6$ and thereafter rapidly decreases to a quasi-constant value at $z/D \sim 9$ and beyond (to $z/D \sim 15$). From these data alone one could partially conclude that the 'hydrodynamic' mixing of the hot and cold jets occurs within two to ten diameters from the exit nozzle. By hydrodynamic we mean just based on velocity data while we acknowledge that the flow is thermal-hydraulic. Interestingly enough, beyond $z/D > 10$ the isothermal single-jet's RMS exceeds that of the thermally stratified triple-jet's ($\Delta T_{\mathrm{hc}} = 5°\mathrm{C}$). Since velocity data of an isothermal triple-jet were not available at present we could not isolate nor fully assess the influence of (thermal) buoyancy on the turbulent mixing process. However, it does not appeal to physical reasoning that an isothermal triple-jet's RMS value would suddenly decrease to less than a single-jet's in comparison. So we believe it likely that either the energy content of the buoyant triple-jet is depleted due to thermal mixing and/or some form of turbulence suppression occurs; that is, something analogous to re-laminarization of turbulent mixed convection flow near the laminar-to-turbulent transition.

3.3. Temperature data

We next present in Fig. 10(a) and (b) the spanwise average temperature and its associated standard deviation profiles at representative axial locations. Here the exit velocities for all three jets are equal, $V_{exit} = 0.5$ m/s, and the hot-to-cold temperature difference is $\Delta T_{hc} = 5°C$. Several

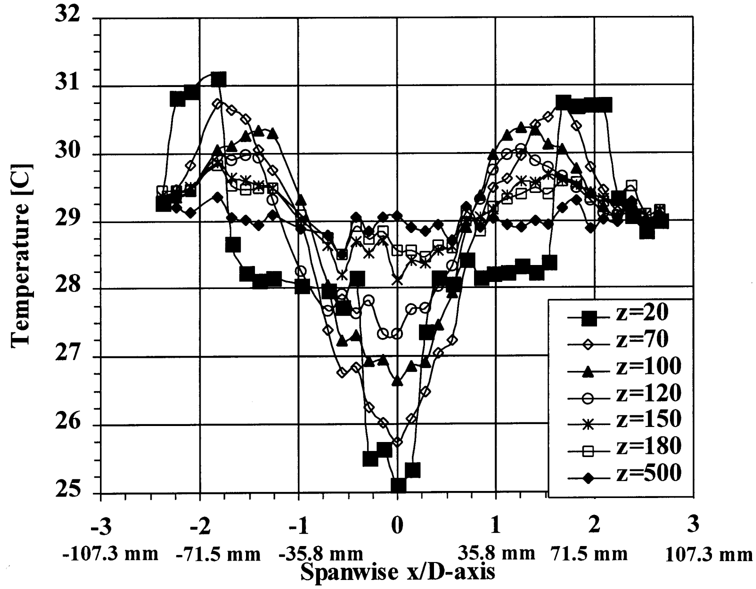

(a) Average temperature

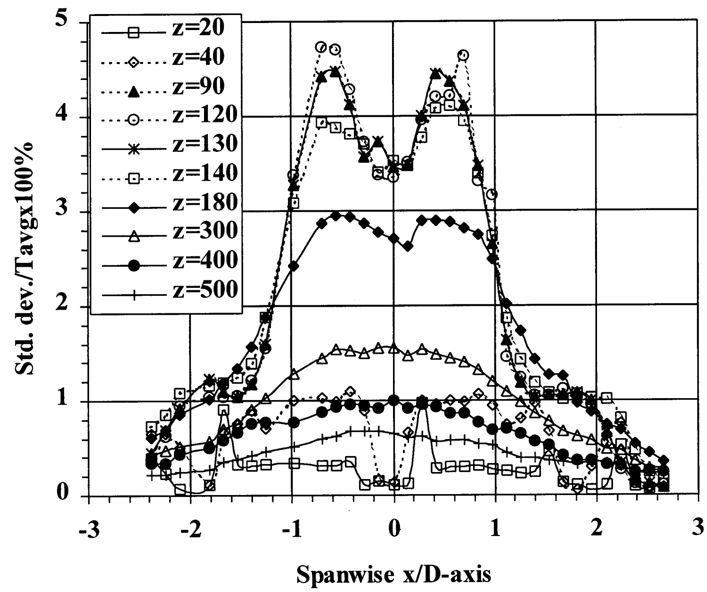

(b) Standard deviation

Fig. 10. Profiles of the average and standard deviation of temperature of the triple-jet at representative axial locations. Isovelocity $\Delta T_{hc} = 5°C$.

points at left are missing due to malfunctioning thermocouples. Each point represents a temperature averaged over $t \sim 20.5$ s containing 1025 samples. The axial distances were selected for clarity in presentation and to correspond where possible to the velocity profile locations. Note that at $z = 20$ (mm) the profile clearly indicates the presence of a central cold jet ($T_c \sim 25.5$°C) and two hot jets ($T_h \sim 30.8$°C), while in-between (at $40 < x < 80$, $110 < x < 150$) the temperature assumes the 'approximate average' of 28°C over a span of 40 mm to either side of the cold jet. Near the region of the individual jets, the temperature gradient is very sharply defined. Further downstream, at $z = 70$, 100, 120 mm, the 'mixing' of the thermally stratified streams is under way as the gradient between the hot and cold jets incrementally decrease. By $z = 180$ then, the temperature gradient between the hot/cold jet do not appreciably differ from that at $z = 500$. Therefore except for $z = 500$ we have not shown the profiles at $z = 200$, 300 and 400 mm. From $z = 20$ to 180, the axial center of the cold jet has increased in temperature (from 25.5°C) to nearly 29°C while the hot jets have decreased in temperature from 30.8 to 29.5°C, a smaller absolute change than for the cold jet. The obvious reason for this is the presence of two hot jets which transfer heat to the single cold jet.

As for Fig. 10(b) the selected z-locations show the gradual change near the exit ($z = 20$, 40 mm) and at or near the maximum magnitude ($z = 120$, 130, 140 mm). The profile show for example at $z = 20$ show the edge of the jets, similar to Fig. 8(c) for velocity, and the core region as well. At $z = 40$, however, the profile in-between the hot/cold jets has already increased relative to the core of the jets. This relative change appears to be an early indication of the thermal mixing at the cold jet at these lower axial locations. By $z = 90$, the relative fluctuation level has increased markedly and the profile itself has changed dramatically. In fact, most of the thermal fluctuations are clearly in between the hot and cold jets. Note too that the relative width of the cold jet's core region remains fairly unchanged (compare $z = 40$, 90) and that a local minimum value exists up to $z \sim 140$ but no longer at $z = 180$. This means, at least qualitatively, that the thermal mixing does not have to encompass (spanwise) the core of the cold jet within $z \leq 140$. This is, however, no longer the case at $z = 180$ where the 'defect' seen at $z < 140$ has all but disappeared. Beyond $z =$ 180 the profile assumes a gradually decreasing Gaussian-like distribution up to and including $z = 500$.

Next, in Fig. 11(a) and (b) we show the temperature profile at three selected downstream locations; one position near the exit, one within the 'onset' of the mixing region and the last in the upper reaches of the mixing region. These regions are further descriptively qualified in the subsequent figures. In the figure, (a) represents cases of equal velocity (isovelocity) with $\Delta T_{hc} = 5°$ or 10° while in (b) ΔT_{hc} remains the parameter, but the heated/unheated jet velocities are dissimilar (non-isovelocity). We define the cold-to-hot velocity ratio, $r = V_{cold,exit}/V_{hot,exit}$ for the purpose of discussion. The non-isovelocity ratio is here fixed at $r = 0.5$. The shaded rectangular blocks which are shown below the abscissa (and in subsequent figures) define the approximate location of the jet exits with respect to the temperature profiles. The contrasting feature between (a) and (b) is the lack of symmetry when $r = 0.5$, the influence of which is duly noted in the relative changes and gradients along the profiles. In fact, from this figure alone one can partially conclude that non-isovelocity delays the mixing process as larger temperature gradients are maintained for identical z/D locations. This observation appears to be consistent with the apparent length to mixing shown in Fig. 5. The asymmetry at $z/D = 2.80$ in (b) however, changes to a symmetric profile by $z/D = 4.19$. This indicates that in spite of non-isovelocity and any consequential delay, mixing eventually occurs between the jets and symmetry in the temperature profile is restored.

Fig. 12(a) and (b) show the axial development of temperature for x/D positions corresponding to the centerline of respectively the left ($x/D = -1.82$), center ($x/D = 0$) and right ($x/D = 1.82$) jets. The temperature difference, ΔT_{hc}, again serves as parameter while (a) and (b) respectively show isovelocity and non-isovelocity cases. We note in general, the profiles suggest three regions of flow

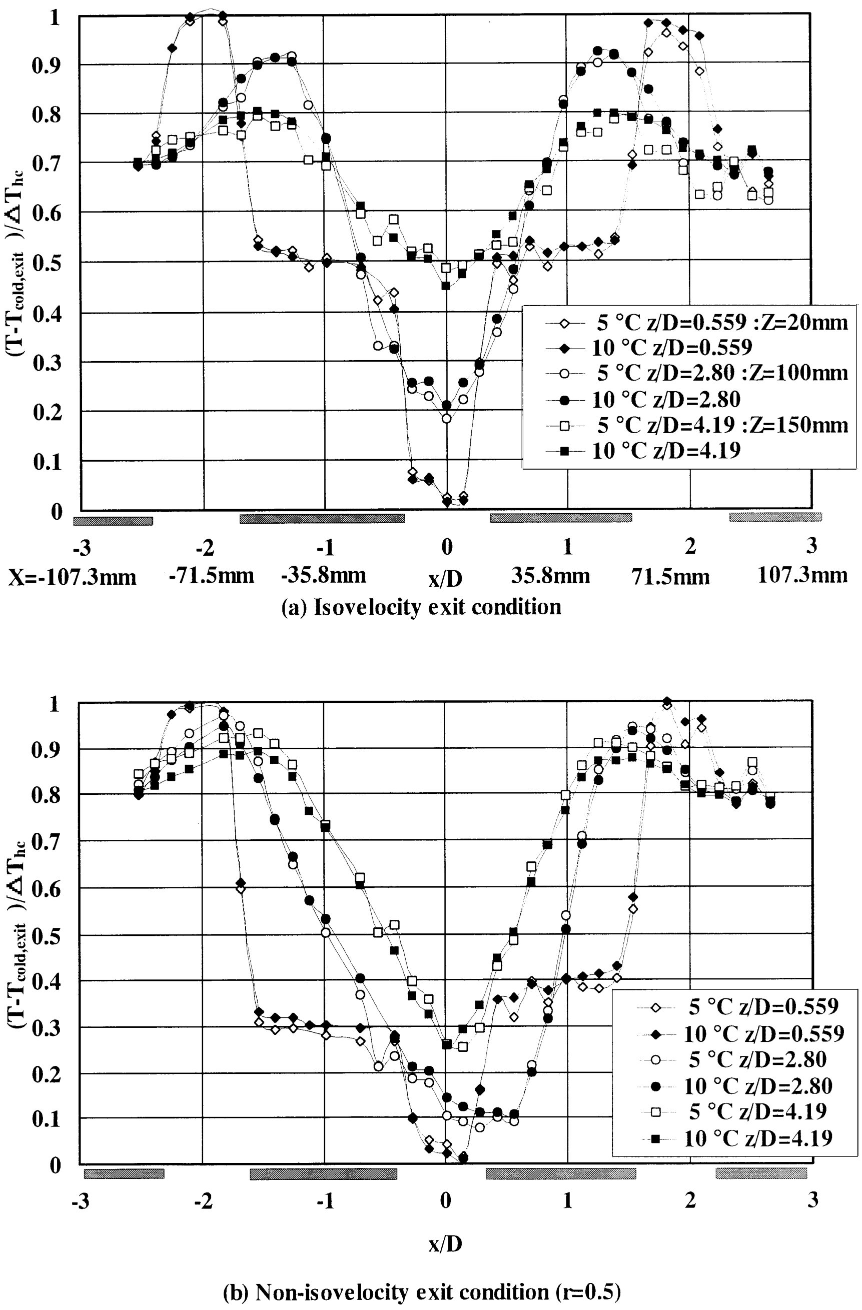

Fig. 11. Temperature profiles under various heated-to-unheated jet temperature differences and isovelocity and non-isovelocity conditions.

as follows: (1) an 'entrance' region ($z/D \leq 2.5$) where the temperature is constant or the temperature increase (unheated jet) or decrease (heated jet) is small; (2) a 'convective mixing' region ($2.5 \leq z/D \leq 7$) where the temperature increase/decrease is significant; and (3) the 'post mixing' region ($z/D \geq 7$) where the temperature assumes an asymptotic trend. There is only a slight difference between $\Delta T_{hc} = 5°$ and 10°C for the heated jets while for the unheated jet, some differences are noticeable just beyond the convective mixing region ($10 < z/D < 17$ for both $r = 1.0$ and $r = 0.5$). The contrasts due to the non-isovelocity itself are: (1) the initial step increase in temperature ($1.8 \leq z/D \leq 3.8$); (2) the relative axial positions where the convective to post-mixing

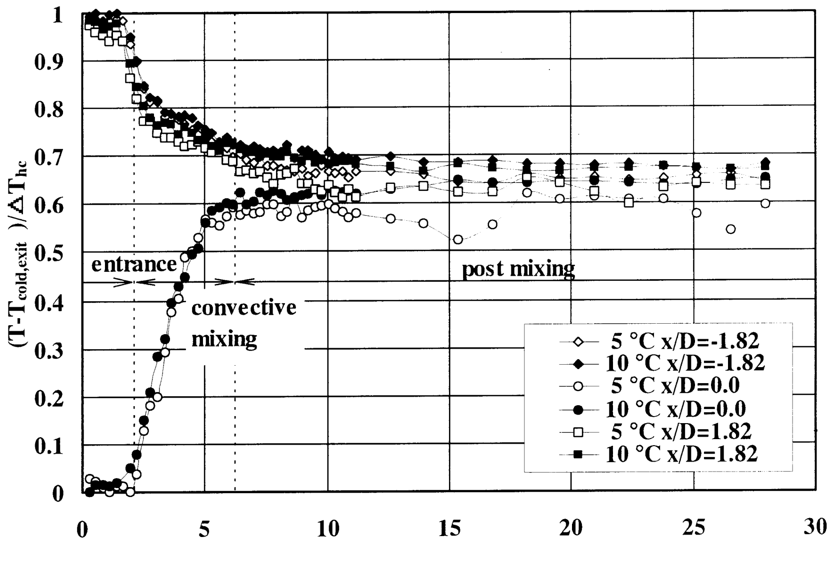

(a) Isovelocity exit condition

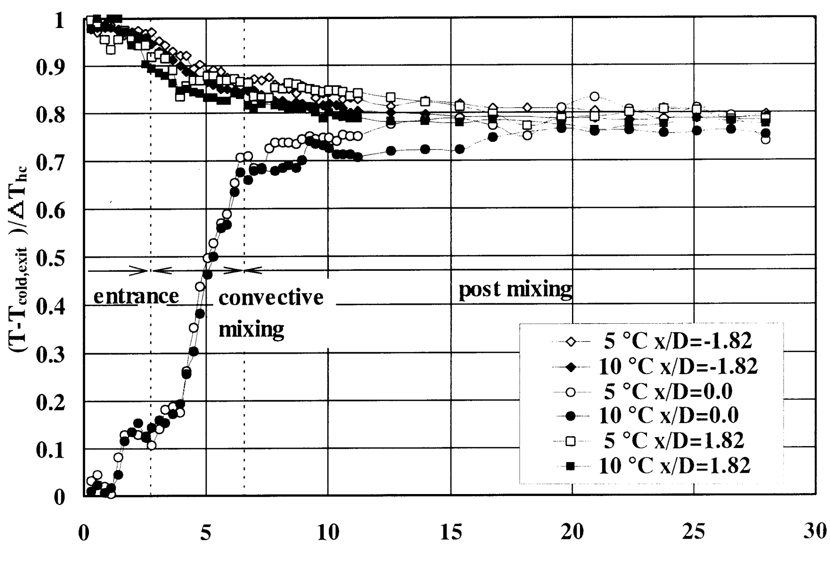

(b) Non-isovelocity exit condition (r=0.5)

Fig. 12. Axial temperature profiles under various heated-to-unheated jet temperature differences and isovelocity and non-isovelocity conditions.

'transition' occur (i.e. $z/D \sim 5$ for $r = 1.0$; $z/D \sim 7.5$ for $r = 0.5$); and (3) the final post-mixing temperatures reached. Surprisingly, the rate of increase in temperature of the unheated jet is very similar for both $r = 1.0$ and $r = 0.5$. This can be interpreted on the one hand to mean that once mixing begins the resulting increase in temperature is relatively independent of the isovelocity or non-isovelocity condition. Viewed in another way, until some unspecified 'hydrodynamic' condition is met (since ΔT_{hc} values are the same), mixing does not occur to any extent such that the spanwise averaged temperature changes. If this train of thought follows, then non-isovelocity essentially delays the hydrodynamic condition that is conducive to thermal mixing; that is, whether this be in the development of the critical size of the vortices created by the mixing layer and/or the characteristic time associated with its development, isovelocity fulfills this criterion earlier than non-isovelocity relative to the exit condition. Recall that a mixing layer in this application describes the dynamics of the interface (edge of the jet) between parallel streams of fluid at either the same or different velocities and temperatures.

Fig. 13(a) and (b) show the RMS temperature plots associated with the average temperature in Fig. 11(a) and (b) at the exact same locations. Fig. 13(a) depicts the expected symmetry in the profiles for the isovelocity case and shows a large increase in $T'_{RMS}/\Delta T_{hc}$ from the exit ($z/D = 0.559$) to $z/D = 2.80$, followed by a slight decrease at $z/D = 4.19$. In contrast in Fig. 13(b), the initially similar profile at the exit changes to an asymmetric profile at $z/D = 2.80$ with a bias toward the right jet and overall, is smaller in magnitude than its isovelocity counterpart. Recall here that $V_{cold,exit} = 0.5$ m/s while $V_{hot,exit} = 1.0$ m/s. By $z/D = 4.19$, however, the symmetry in the profile has returned. We note too that in contrast, isovelocity produces a larger difference in $T'_{RMS}/\Delta T_{hc}$ between 5°C and 10°C than under non-isovelocity. In fact since $T'_{RMS}/\Delta T_{hc}$ is larger at 5°C, this may indirectly mean that locally, as in Sakakibara et al. (1993) relative buoyancy suppresses turbulent fluctuations and thus T'_{RMS}. At the same time, the lack of any difference in non-isovelocity equally suggests that indeed inertial effects, mainly those attributable to $r = 0.5$, compensates the increase in buoyancy between 5°C and 10°C. Since however, the initiation of convective mixing results in a symmetric profile, mixing obviously undermines the origins of asymmetry appearing at $z/D = 2.80$.

As for the axial distribution, Fig. 14(a) and (b) show a precipitous increase in $T'_{RMS}/\Delta T_{hc}$ up to $z/D \sim 5$ and then an equally sharp drop to $z/D \sim 10$, from where there is a gradual decay to $z/D \sim 28$. The contrasting feature attributable to non-isovelocity here seems to be at $2 < z/D < 3$, where there is a short-lived increase to a plateau, followed by a slight decrease and then smaller axial length over ($z/D > 3$) which $T'_{RMS}/\Delta T_{hc}$ increases to its maximum and then decays. This last observation also means that the z/D location at which a given post-mixing $T'_{RMS}/\Delta T_{hc}$ magnitude is jointly reached occurs earlier in non-isovelocity than isovelocity. One may conclude from these plots that non-isovelocity tends to alter the thermal mixing process by delaying its inception, but once initiated compacts the axial length over which mixing takes place in contrast to the isovelocity case.

Fig. 15(a) and (b) depict profiles of the spanwise and axial average temperatures for one isovelocity and two non-isovelocity cases. The axial position in (a) is $z/D = 2.8$ while, for (b), the centerline of the unheated jet ($x/D = 0$) has been selected. As we previously said non-isovelocity, $r = 0.5$ or 0.7, introduces asymmetry in the spanwise profiles such that the onset (location) of thermal mixing is displaced slightly downstream (z/D). As a result, Fig. 15(b) shows that the post-mixing temperature or the final equilibrium temperature is also elevated with non-isovelocity. One reason for the difference in the onset of mixing can be seen in Fig. 16(a) where for both non-isovelocity cases, the normalized T'_{RMS} is neither symmetrically distributed nor of magnitude as large as that for $r = 1.0$. Thus, even though the spanwise averaged T'_{RMS} reaches a value as large as the isovelocity case in Fig. 16(b), mixing in the spanwise direction is not as 'efficient' initially as when the jets are under isovelocity condition.

Fig. 17(a) and (b) equally supports a view toward three regions of flow and simultaneously

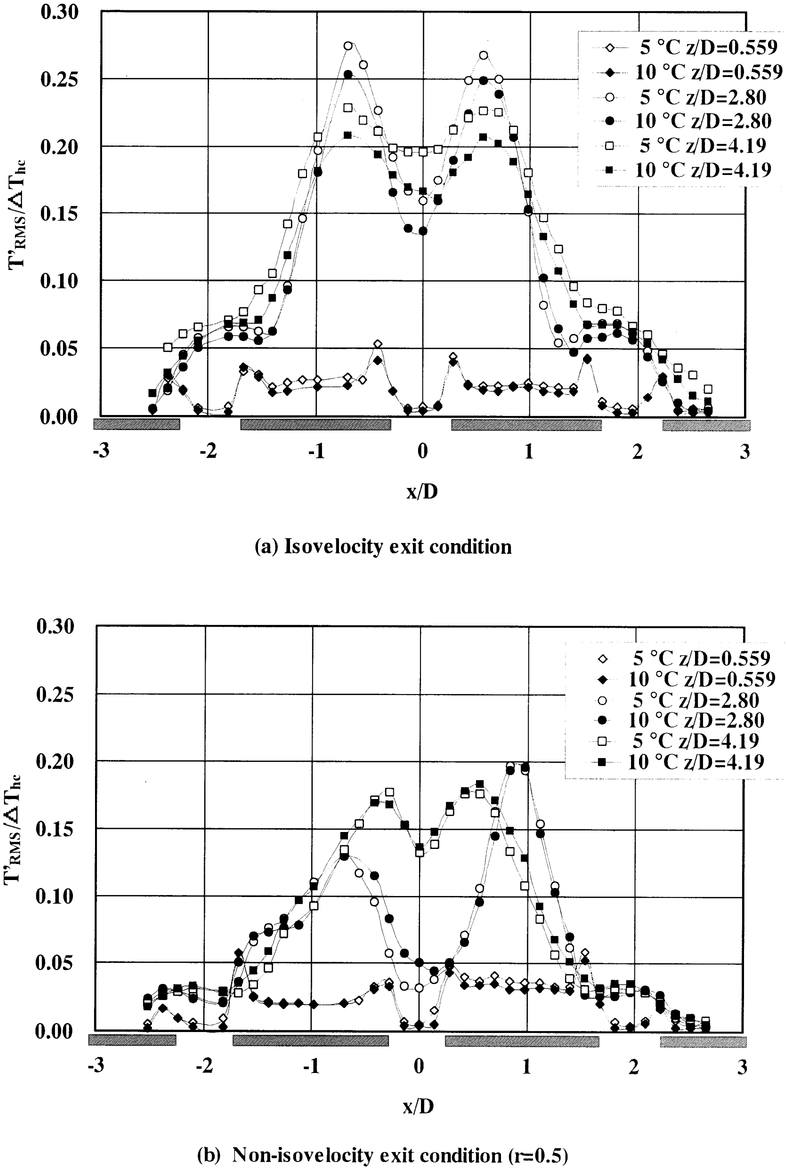

Fig. 13. Profiles of the root-mean-square of temperature, T'_{RMS}, under various heated-to-unheated jet temperature differences and isovelocity and non-isovelocity conditions.

exhibits the distinction between isovelocity and non-isovelocity flows, as well as that between single- and triple-jets. The data has been plotted in terms of a normalized ΔT_{hc} versus the axial distance, z/D, modified by the ratio of heated-to-unheated jet densities ($\rho_{hot,exit}/\rho_{cold,exit}$). In the same figure, the buoyant single-jet data of Kataoka and Takami (1977) with a slightly different definition of temperatures has been plotted. In Kataoka's case, the ordinate is the ratio $(T_{centerline} - T_{bulk})/(T_{max} - T_{bulk})$, where $T_{centerline}$, T_{max} and T_{bulk} are respectively the jet's centerline temperature, the maximum temperature in the transverse direction (spanwise) and the bulk temperature.

Regarding our data, one can see that although the velocity ratio, r (=1.0 or 0.5), alters the trends in the data, three regions of flow are clearly well-defined. In particular, the second region where the temperature precipitously increases [case (a): $2<(\rho_{hot,exit}/\rho_{cold,exit})^{1/2}\ z/D<6$; case (b): $4<(\rho_{hot,exit}/\rho_{cold,exit})^{1/2}\ z/D_h<7$] corresponds to the convective mixing region. Equally, the entrance region is $(\rho_{hot,exit}/\rho_{cold,exit})^{1/2}\ z/D_h<2$ and the post-mixing region is $(\rho_{hot,exit}/\rho_{cold,exit})^{1/2}\ z/$

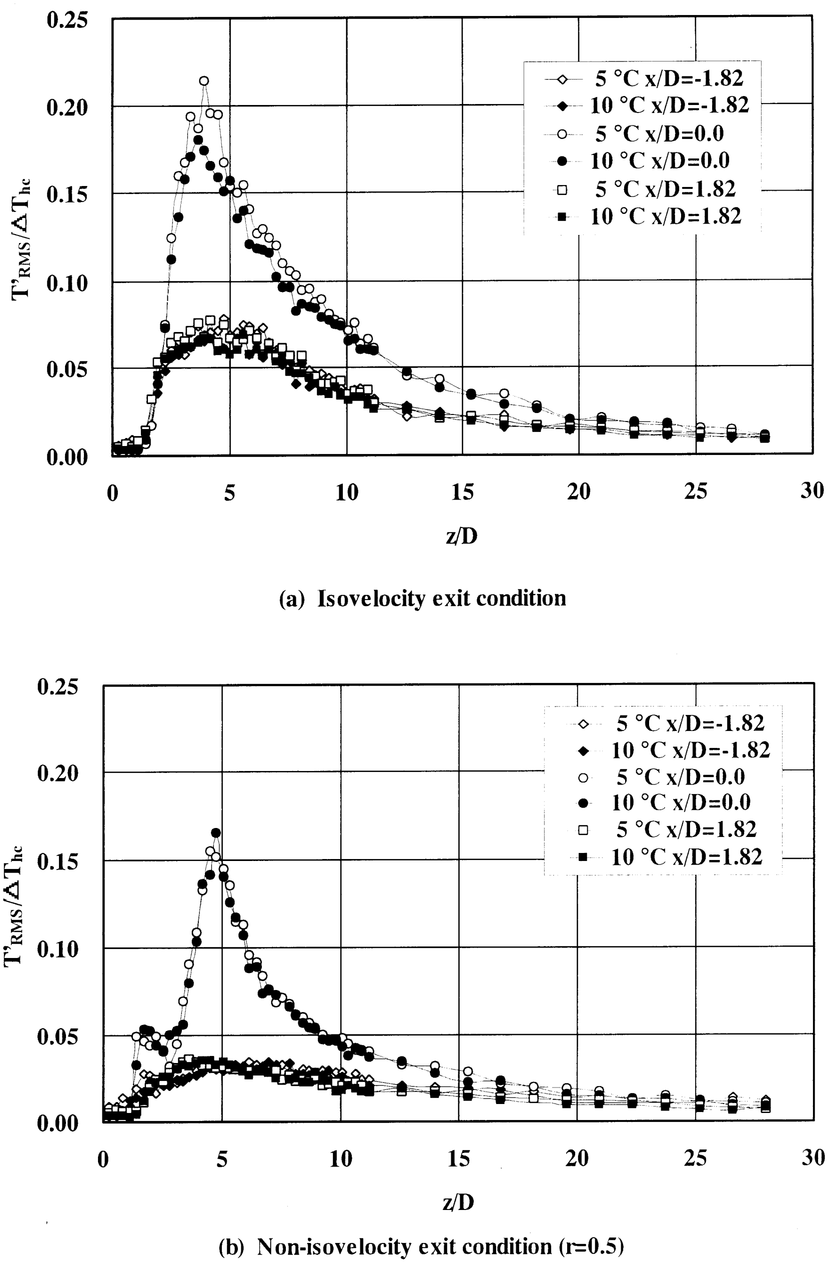

Fig. 14. Axial RMS temperature profiles under various heated-to-unheated jet temperature differences and isovelocity and non-isovelocity conditions.

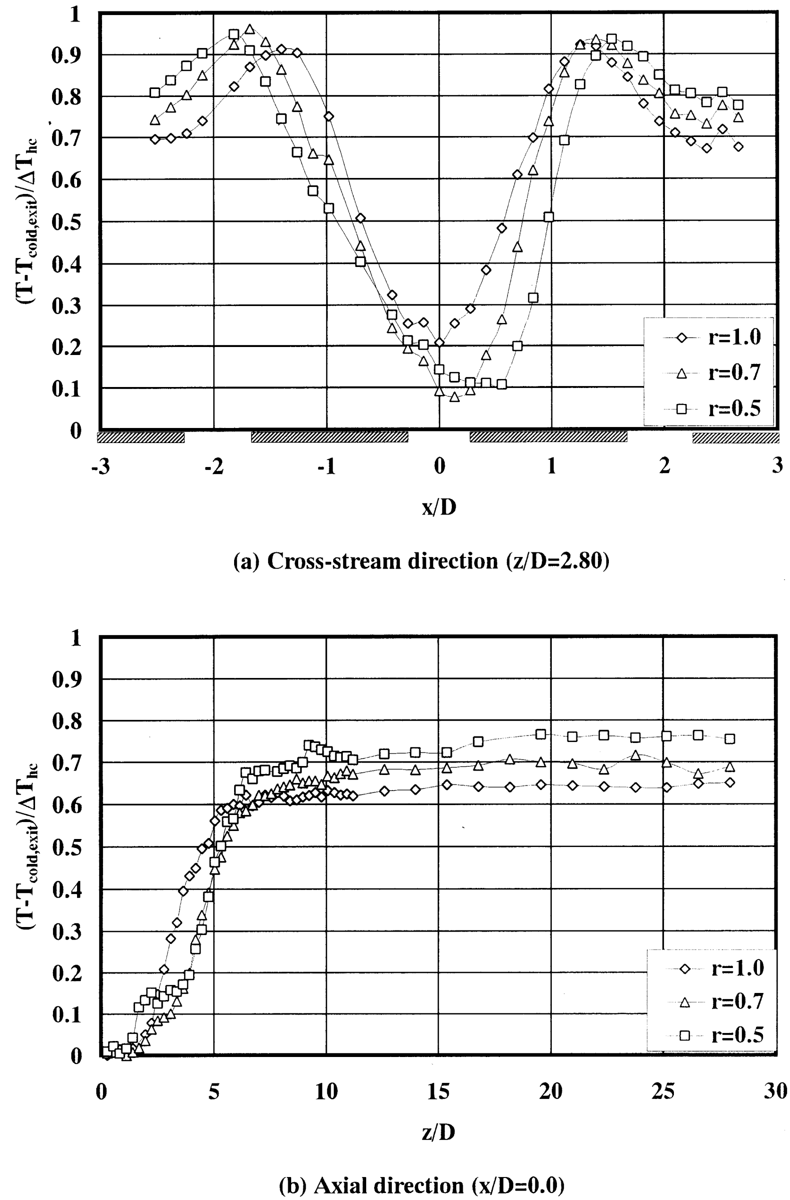

Fig. 15. The influence of non-isovelocity on the cross-stream and axial temperature profiles ($\Delta T_{hc} = 10°C$).

> 6 in Fig. 17(a). The observed shift downstream in the beginning of the convective mixing region in (b) is evidently due to non-isovelocity itself as discussed. A comparison of the slope of the regression line drawn through the convective mixing region's points and that representing Kataoka's data clearly exhibits a difference between the single- and triple-jet. That is, in that the slope reflects the intensity of mixing (and indirectly turbulence) between the jets in some sense, the ordered magnitude of their respective slopes (0.215 single-jet, 0.430 isovelocity, 0.632 non-isovelocity) confirms our assertions to this point; that is, for our triple-jet arrangement, a difference in jet velocities hydrodynamically shifts the onset location of mixing, and compacts the axial distance over which thermal mixing takes place.

Finally in Fig. 18 we show an iso-contour plot of the calculated turbulent heat flux distribution defined as, $Q_{turb} \equiv \rho C_p u'_{RMS} T'_{RMS}$. Since u'_{RMS} and T'_{RMS} were measured separately as a function of (x,z), the figure represents a semi-quantitative estimate of Q_{turb}. The purpose of the figure from the perspective of the thermal striping issue, is to identify the convective mixing region. The thermo-physical properties, ρ and C_p, were evaluated at the local temperature. The iso-contour plot shown is for velocity and temperature differ-

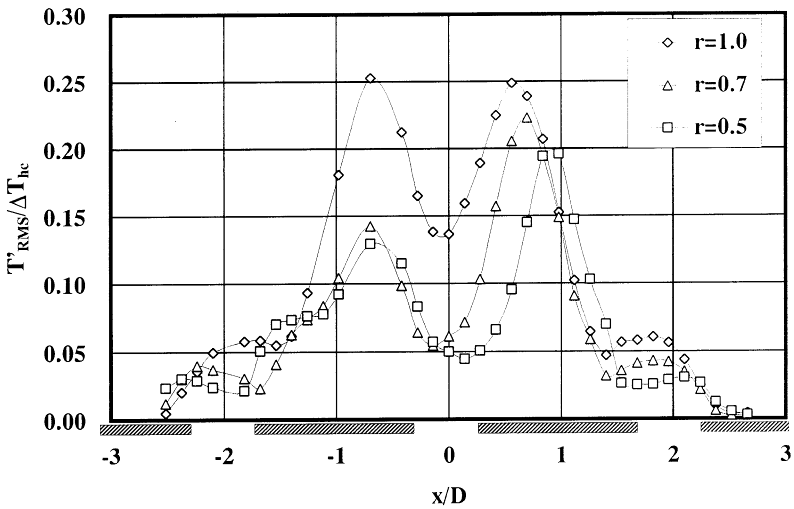

(a) Cross-stream direction (z/D=2.80)

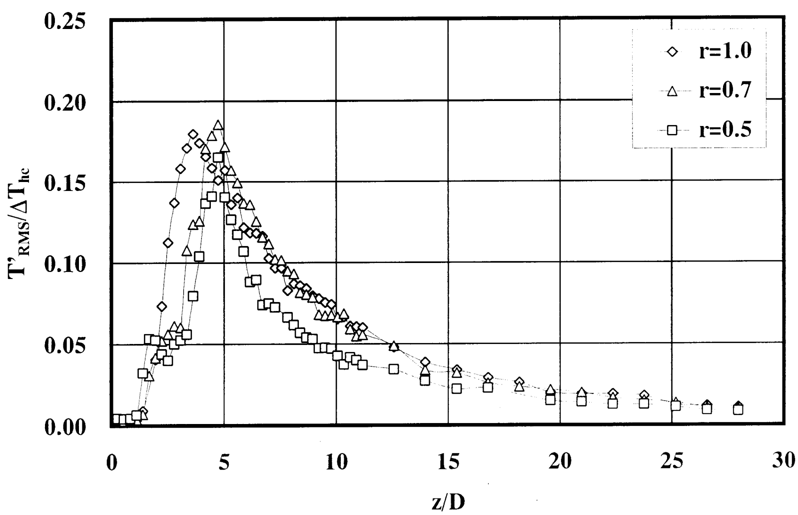

(b) Axial direction (x/D=0.0)

Fig. 16. The influence of non-isovelocity on the cross-stream and axial RMS temperature profiles ($\Delta T_{hc} = 10°C$).

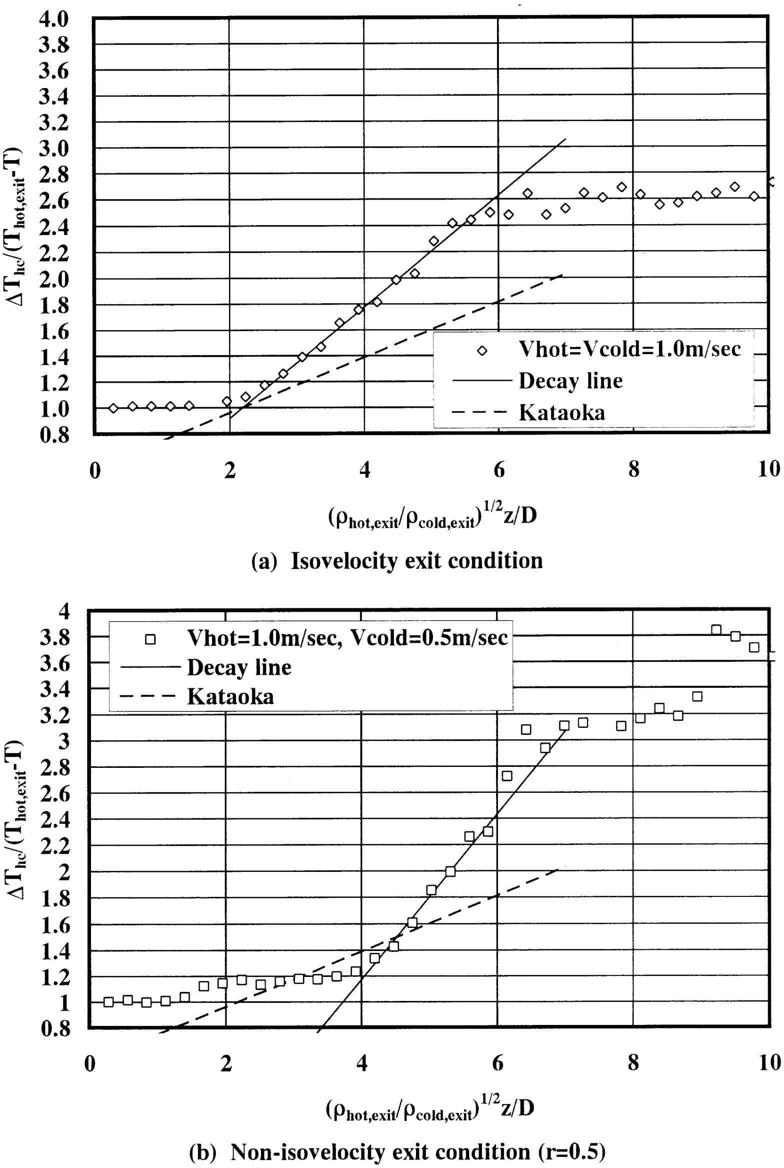

Fig. 17. A comparison of temperature decay trends with axial distance for single- and triple-jets ($\Delta T_{hc} = 10°C$, $x/D = 0.0$).

ence, $V_{cold,exit} = V_{hot,exit} = 0.5$ m/s and $\Delta T_{hc} = 5°C$, with the axis of the left, center and right jet exits located approximately at $x/D \sim -2.0, 0.0, +2.0$. Recall that the quantity u'_{RMS} is not strictly the x-component of velocity fluctuation since the UVP-TDX was oriented at 10° with respect to the horizontal; that is, it includes primarily the u'_{RMS} component, but also a small contribution from w'_{RMS}. In addition, since the traversed increments for temperature and velocity were of different sizes, some interpolation had to be performed in order to fill-in missing data. As a matter of approach, the coarser (larger traverse increments) temperature data was taken as the basis onto which the finer velocity data was adapted, so that interpolation would be minimized. Fortunately, both the temperature and velocity data have nearly equivalent resolution up to $z \sim 275$ ($z/D \sim 7.7$), which also happens to be the region of relevance for thermal mixing. It is clear from the figure that beyond $z \sim 300$ ($z/D \sim 8.4$), the distribution shows largely linear patterns (straight lines) which are the result of sparsely recorded data points and interpolation between these points.

It is by coincidence that the spanwise turbulent heat flux is the one estimated and is also the quantity which may hold more significance in terms of evaluating the thermal mixing. That is, if the spanwise mixing is efficient and the thermal energy is well distributed, the thermal striping impact is lessened on any solid boundary which the flow encounters. In other words, at a given axial location, the uniformity in the spanwise temperature distribution is a measure of the thermal mixing which has taken place below it. So in spite of the compromises made in matching the velocity and temperature fields, the figure supports our view that there is significant convective mixing of the two heated jets, as opposed to thermal striping, within an identifiable downstream distance. In the present case, for an average exit nozzle velocity of $V_{\mathrm{cold}} = V_{\mathrm{hot}} = 0.5$ m/s and $\Delta T_{\mathrm{hc}} = 5°\mathrm{C}$, convective mixing takes place over $70 \leq z \leq 160$ mm or when non-dimensionalized by the hydraulic diameter, $z/D \sim 2.0$ to 4.5. In addition, in the spanwise direction most of the mixing takes place over $x/D \leq |2.25|$, centered about the axis of the central (cold) jet; that is, mixing takes place between the hot and cold jets.

4. Conclusions

An experiment investigating the thermal-hydraulic mixing of three quasi-planar, vertically flowing (water) jets was conducted. In the experiment the central jet was unheated (cold) and therefore non-buoyant, while the two adjacent jets were heated (hot) and therefore buoyant. The three jets flowed into a large volume of water initially at the central jet's temperature. The ratio of the cold-to-hot jets' average exit velocities (and flowrate) was equal to $r = V_{\mathrm{cold,exit}}/V_{\mathrm{hot,exit}} = 1.0$ (isovelocity), 0.7 or 0.5 (both non-isovelocity). The temperature difference between the cold and hot jets was $\Delta T_{\mathrm{hc}} = 5°\mathrm{C}$ or 10°C. The typical Reynolds number was, $Re \equiv VD/\nu = 1.8 \times 10^4$, where D is the hydraulic diameter of the exit nozzle. Velocity measurements were taken using

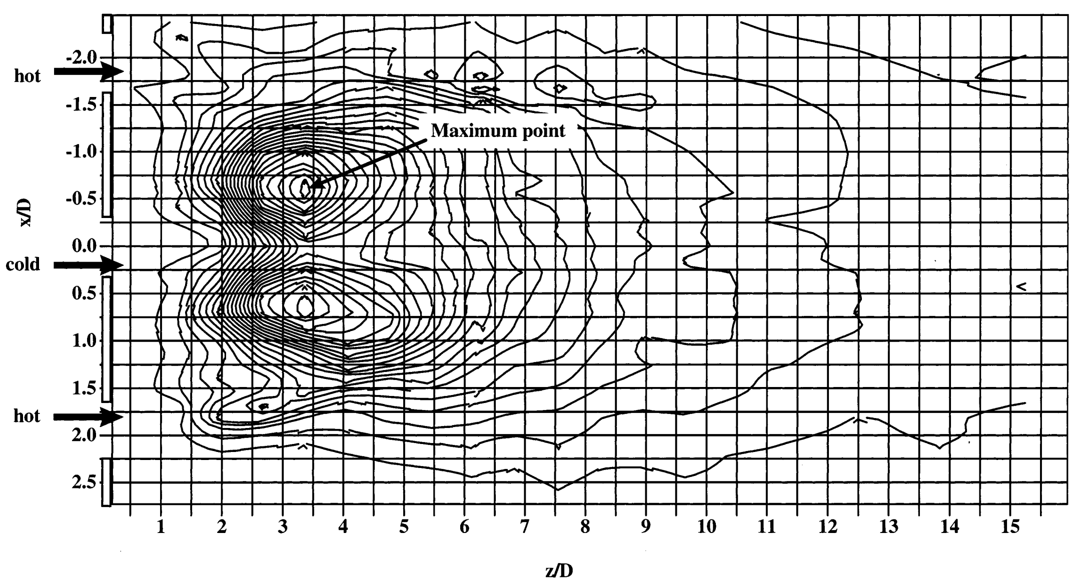

Fig. 18. Estimated turbulent heat flux distribution for T05 V0505 (scale is 2.0E4–4.6E5 W/m^2).

an ultrasound Doppler velocimeter (UDV), only for case $V_{cold} = V_{hot} = 0.5$ m/s and $\Delta T_{hc} = 5°C$, while temperature data were taken from a vertically traversed array of 39 thermocouples. The UDV yielded velocity profiles consisting of 128 points along its measurement line, which were collected from the echo signals received from ultrasound reflecting particles moving with the flow. The measured velocities represented nearly the spanwise (transverse) component of flow, as the ultrasound beam was directed at a 10° angle with respect the horizontal. Except for some apparent difficulty in the echo signal processing (amplification) in the region closest to the transducer, both single- and triple-jet configurations revealed satisfactory velocity data. In fact, a comparison of the centerline decay velocity of our single-jet was in agreement with past trends for planar gas jet.

In contrast to the single-jet, UDV measurements of the triple-jet showed large velocity fluctuations expressed in terms of the standard deviation of the average velocity. In fact, in comparison to the single-jet, the normalized RMS were as much as 20 times as large in the region in-between the hot and cold jets. The axial distribution of the RMS further localized this hydrodynamically based mixing region. The scalar component, temperature equally reflected these trends for the isovelocity case while for non-isovelocity, a localized asymmetry in the spanwise profiles appeared to delay the 'onset' of convective, thermal mixing. However, mixing did eventually occur under non-isovelocity and while in the 'post-mixing' region symmetric temperature profiles returned, slightly higher post-mixing temperatures we observed. Finally, for the representative isovelocity case, $V_{cold,exit} = V_{hot,exit} = 0.5$ m/s and a hot-to-cold jet temperature difference $\Delta T_{hc} = 5°$ (30°C and 25°C), a contour plot of the estimated turbulent heat flux showed that most of the convective mixing between jets occurs over an axial distance of $z/D \sim 2.0$ to 4.5, centered about the axis of the cold jet, over a width, $x/D \leq |2.25|$. Thus given UVP-based velocity and temperature data, it is possible not only to identify the convective mixing process, but to localize the spatial extent of this convective mixing.

5. Nomenclature

D	hydraulic diameter of the inlet channel (mm)
ML	measurement length; pertaining to ultrasonic beam path
Q_{turb}	turbulent heat flux, turbulent heat flux at exit, $= \rho C_p\ u'_{RMS}\ T'_{RMS}$
r	cold-to-hot jet average velocity ratio at exit, $= V_{cold,exit}/V_{hot,exit}$
R, L	from right, from left
Re	Reynolds number of inlet channel, $= (UD/\ v)$ or $(Uz/\ v)$
SD	standard deviation of average velocity
TDX	transducer
T	temperature (°C)
$T_{h(ot)}$	temperature of 'hot' jet (°C)
$T_{c(old)}$	temperature of the 'cold' jet (°C)
ΔT_{hc}	temperature difference between hot and cold jets (°C)
T'_{RMS}	root-mean-square temperature (°C)
T_{avg}	average temperature (°C)
T_{exit}	exit temperature (°C)
u_x or U_x	local axial average velocity (mm/s)
u'_{RMS} or U_{rms}	root-mean-square velocity (mm/s)
U_{av}	average velocity (mm/s)
U_o	velocity at the exit of the nozzle (mm/s)
$U_{ctr,max}$ or U_m	maximum centerline velocity of profile (mm/s)
UVP	ultrasound velocity profile monitor
$V_{cold,exit}$, $V_{hot,exit}$	average exit velocity of cold and hot jets
x, z	spanwise or cross-stream and axial coordinates
x/D, z/D	spanwise (transverse) and axial coordinates normalized by hydraulic diameter
z_{uc}	velocity core length

Greek symbols

$\rho_{cold,exit}$, $\rho_{hot,exit}$	density of cold and hot jets, (kg /m^3)

Acknowledgements

The first author would like to thank PNC for his appointment as PNC International Fellow. The authors also acknowledge the efforts of Mr Miyakoshi, Mr Itoh and Mr Onuma who initiated and conducted the experimental measurements, maintained the data and prepared the UVP and temperature data which were analyzed in order to prepare this report.

References

Betts, C., Bourman, C., Sheriff, N., 1983. Thermal striping in liquid metal cooled fast breeder reactors. In: 2nd International Topical Manufacturing on Nuclear Reactor Thermal Hydraulics, NURETH-2, Santa Barbara, CA, vol. 2, pp. 1292–1301.

Brunings, J.E., 1982. LMFBR thermal-striping evaluation. Interim report, Research Project 1704-11, prepared by Rockwell International Energy Systems Group, Canoga Park, CA, EPRI-NP-2672, October 1982.

Gebhardt, B., Jaluria, Y., Mahajan, R.L., Sammakia, B., 1988. Buoyancy-Induced Flows and Transport, reference ed. Hemisphere Publishing Corporation, New York, pp. 657–697.

Kataoka, K., 1986. Modeling turbulent jets with variable density. In: Cheremisinoff, N.P. (Ed.), Encyclopedia of Fluid Mechanics, Dynamics of Single-Fluid Flows and Mixing, vol. 2. Gulf Publishing, Houston, pp. 511–543.

Kataoka, K., Takami, T., 1977. Experimental study of eddy diffusion model for heated turbulent free jets. Am. Inst. Chem. Eng. J. 23, 889–896.

Moriya, S., Ushijima, S., Tanaka, N., Adachi, S., Ohshima, I., 1991. Prediction of thermal striping in reactors. International Conference Fast Reactors and Related Fuel Cycles, 28 October–1 November, Kyoto, 1991, Vol. 1, pp. 10.6.1–10.6.10.

Muramatsu, T., 1994. Development of thermohydraulics computer programs for thermal striping phenomena. Specialists meeting on correlation between material properties and thermohydraulics conditions in LMFRs, IAEA Working Group on Fast Reactors, IWGFR/90, Aix-en-Provence, 22–24 November 1994.

Sakakibara, J., Hishida, K., Maeda, M., 1993. Measurement of thermally stratified pipe flow using image-processing techniques. Exp. Fluids 16, 82–96.

Takeda, Y., 1986. Velocity profile measurement by ultrasound Doppler shift method. Int. J. Heat Fluid Flow 8, 313–318.

Takeda, Y., 1991. Development of an ultrasound velocity profile monitor. Nucl. Eng. Design 126, 277–284.

Takeda, Y., 1993. Velocity profile measurement by ultrasonic Doppler method. In: Kellher, M.D., et al. (Eds.), Proceedings 3rd World Conference on Experimental Heat Transfer, Fluid Mechanics and Thermo., Honolulu, 31 October–5 November 1993, pp. 126–131.

Tenchine, D., Moro, J.-P., 1995. Comparative analysis of sodium and air mixing jets experiments. 8th IAHR Working Group Mtg. Adv. Nucl. React. Thermohydraulics, 13–15 June 1995, Řež, Czech Republic.

Tenchine, D., Nam, H.-Y., 1987. Thermal hydraulics of co-axial sodium jets. Am. Inst. Chem. Eng. Symp. Ser. 83 (257), 151–156.

Tokuhiro, A., 1996. Investigation of free and forced flows of relevance to fast reactor thermohydraulics using the ultrasonic Doppler method. 1st Int. Symp. on Ultrasonic Doppler Methods for Fl. Mech. and Fl. Eng., Paul Scherrer Institute, Villigen, 9–11 September 1996.

D.S. Wood, Proposal for design against thermal striping, Nuclear Energy, 19, no. 6 (1980) 433-437.